

LETTER TO THE EDITOR

Fast infrared winds during the radio-loud and X-ray obscured stages of the black hole transient GRS 1915+105

J. Sánchez-Sierras^{1,2}, T. Muñoz-Darias^{1,2}, S. E. Motta^{3,4}, R. P. Fender^{4,5}, A. Bahramian⁶, C. Martínez-Sebastián^{1,2}, J. A. Fernández-Ontiveros⁷, J. Casares^{1,2}, M. Armas Padilla^{1,2}, D. A. Green⁸, D. Mata Sánchez^{1,2}, J. Strader⁶, and M. A. P. Torres^{1,2}

¹ Instituto de Astrofísica de Canarias, c/Vía Láctea, S/N, E-38205 La Laguna, Tenerife, Spain

² Departamento de Astrofísica, Universidad de La Laguna, E-38206 La Laguna, Tenerife, Spain

³ Osservatorio Astronomico di Brera, Via E. Bianchi 46, I-23807 Merate (LC), Italy

⁴ Department of Physics, University of Oxford, Denys Wilkinson Building, Keble Road, Oxford OX1 3RH, UK

⁵ Department of Astronomy, University of Cape Town, Private Bag X3, Rondebosch 7701, South Africa

⁶ International Centre for Radio Astronomy Research, Curtin University, GPO Box U1987, Perth, WA 6845, Australia

⁷ Centro de Estudios de Física del Cosmos de Aragón (CEFCA), Plaza San Juan 1, 44001 Teruel, Spain

⁸ Astrophysics Group, Cavendish Laboratory, 19 J. J. Thomson Avenue, Cambridge CB3 0HE, UK

December 8, 2023

ABSTRACT

The black hole transient GRS 1915+105 entered a new phase of activity in 2018, generally characterised by low X-ray and radio fluxes. This phase has only been interrupted by episodes of strong and variable radio emission, where high levels of X-ray absorption local to the source were measured. We present 18 epochs of near-infrared spectroscopy (2018–2023) obtained with GTC/EMIR and VLT/X-shooter, spanning both radio-loud and radio-quiet periods. We demonstrate that radio-loud phases are characterised by strong P-Cygni line profiles, indicative of accretion disc winds with velocities of up to $\sim 3000 \text{ km s}^{-1}$. This velocity is consistent with those measured in other black hole transients. It is also comparable to the velocity of the X-ray winds detected during the peak outburst phases in GRS 1915+105, reinforcing the idea that massive, multi-phase outflows are characteristic features of the largest and most powerful black hole accretion discs. Conversely, the evolution of the Bry line profile during the radio-quiet phases follows the expected trend for accretion disc lines in a system that is gradually decreasing its intrinsic luminosity, exhibiting weaker intensities and more pronounced double-peaks.

Key words. Accretion, accretion discs – X-rays: binaries – Stars: individual: GRS 1915+105 – Stars: individual: V1487 Aql

1. Introduction

The black hole (BH) transient GRS 1915+105 has the longest orbital period among its class and, consequently, a large and powerful accretion disc ($P = 33.85 \pm 0.16$ days; Steeghs et al. 2013; Corral-Santana et al. 2016). This low-mass X-ray binary (XRB) was discovered in 1992 (Castro-Tirado et al. 1994) during the onset of an outburst. Since then, it has been active for more than 25 years, exhibiting a diverse range of accretion-related phenomena and associated outflows, such as jets and hot X-ray winds (e.g. Mirabel & Rodríguez 1994; Eikenberry et al. 1998; Fender & Belloni 2004; Neilsen & Lee 2009; Neilsen et al. 2011).

In 2018, GRS 1915+105 entered a new phase (see Fig. 1). The X-ray and radio fluxes started to decrease gradually, reaching a plateau stage at low flux. This was followed (May 2019) by a further decline in the observed X-ray emission, which was surprisingly accompanied by an increase in the radio flux back to pre-2018 levels. Strong intrinsic obscuration was inferred from X-ray spectroscopy obtained during this phase, which could qualitatively explain (at least in part) the puzzling behaviour of the source (Miller et al. 2020; Motta et al. 2021; Balakrishnan et al. 2021). This radio-loud phase at low X-ray flux lasted more than two years and it does not have clear precedent in XRBs. Once this phase ended, the source displayed both low X-ray and radio fluxes, consistent with a gradual return towards quies-

cence. Finally, after several months of particularly low activity, the source started a new radio-loud phase in April 2023 (Eggen et al. 2023).

GRS 1915+105 cannot be observed at optical wavelengths due to a very high extinction along the line of sight ($A_V = 19.6 \pm 1.7$; Chapuis & Corbel 2004). Thus, the near-infrared (NIR) offers a unique observing window to study the outer accretion disc and the possible presence of low-ionisation (also known as cold) winds (e.g. Muñoz-Darias et al. 2019; see also Ponti et al. 2012; Díaz Trigo & Boirin 2016; Parra et al. 2023 for hot, X-ray winds). These outflows are particularly conspicuous in other transient XRBs with large accretion discs (e.g. V404 Cyg and V4641 Sgr; Muñoz-Darias et al. 2016, 2017, 2018) and can be associated with high levels of variable, intrinsic X-ray absorption (e.g. Motta et al. 2017a,b). Here, we present near-infrared spectroscopy and photometry of GRS 1915+105 covering the different phases of its 2018–2023 evolution. This is supplemented by contemporaneous X-ray and radio monitoring.

2. Observations and data reduction

2.1. NIR spectroscopy

We present NIR spectroscopy of GRS 1915+105 obtained over 18 epochs between 2018 and 2023 (see Table 1). Eight corre-

Table 1. Spectroscopic epochs and X-ray and radio properties.

Epoch	MJD (date)	Instrument	X-ray [§]	Radio [†]	Bry EW [Å] [‡]	Bry FWHM [km s ⁻¹]	K_s (AB mag)
E-18A	58263.207 (2018-05-25)	GTC/EMIR	high	quiet	10.8 ± 0.7	590 ± 30	14.53 ± 0.12
E-18B	58305.005 (2018-07-06)	GTC/EMIR	high	quiet	9.7 ± 0.6	630 ± 30	–
E-18C	58315.951 (2018-07-16)	GTC/EMIR	high	quiet	6.5 ± 0.9	620 ± 60	–
E-18D	58354.025 (2018-08-24)	GTC/EMIR	high	quiet	3.7 ± 1.2	600 ± 150	–
E-19A	58626.323 (2019-05-23)	VLT/X-shooter	low	loud	66.9 ± 0.1	2090 ± 20	14.18 ± 0.03 ^a
E-19B	58633.308 (2019-05-30)	VLT/X-shooter	low	loud	33.4 ± 0.1	1058 ± 14	~ 14.9 ^b
E-19C	58640.284 (2019-06-06)	VLT/X-shooter	low	loud	59.6 ± 0.1	1740 ± 30	~ 13.6 ^b
E-19D	58659.199 (2019-06-25)	VLT/X-shooter	low	loud	27.5 ± 0.1	813 ± 11	~ 13.9 ^b
E-21A	59446.019 (2021-08-20)	GTC/EMIR	flare	quiet	7.8 ± 0.5	660 ± 40	15.33 ± 0.03
E-21B	59451.095 (2021-08-25) 59451.989 (2021-08-25) 59453.075 (2021-08-27)	GTC/EMIR	flare	quiet	6.1 ± 0.4	486 ± 13	15.10 ± 0.05
E-21C	59476.904 (2021-09-19)	GTC/EMIR	low	quiet	8.4 ± 0.7	810 ± 90	14.82 ± 0.04
E-22A	59828.021 (2022-09-06) 59830.052 (2022-09-08)	GTC/EMIR	low	quiet	< 0.17	–	–
E-22B	59859.906 (2022-10-07) 59891.803 (2022-11-08)	GTC/EMIR	low	quiet	< 0.17	–	15.8 ± 0.2
E-22C	59894.810 (2022-11-11) 59895.811 (2022-11-12)	GTC/EMIR	low	quiet	< 0.17	–	15.7 ± 0.2
E-23A	60076.375 (2023-05-12)	VLT/X-shooter	low	loud	138.3 ± 0.1	641 ± 7	~ 12.7 ^b
E-23B	60082.374 (2023-05-18)	VLT/X-shooter	low	loud	99.1 ± 0.1	626 ± 6	~ 12.2 ^b
E-23C	60094.285 (2023-05-30)	VLT/X-shooter	low	loud	142.7 ± 0.1	674 ± 6	~ 12.3 ^b
E-23D	60161.195 (2023-08-05)	VLT/X-shooter	low	loud	37.31 ± 0.05	620 ± 7	~ 12.9 ^b

[§] The label ‘high’ indicates X-ray fluxes $\geq 0.2 \times 10^{-8}$ erg cm⁻² s⁻¹, whereas ‘low’ corresponds to $< 0.1 \times 10^{-8}$ erg cm⁻² s⁻¹. Observations taken during X-ray flares (‘flare’) have associated fluxes in the range of ~ 0.1 – 0.2×10^{-8} erg cm⁻² s⁻¹ (Fig. 1).

[†] Radio-quiet periods exhibit fluxes of ~ 1 – 5 mJy, whereas radio-loud epochs range from ~ 10 to 2000 mJy (Fig. 1).

[‡] We define EW as positive in emission.

^a From the value $K_s = 12.33 \pm 0.03$ (Vega) obtained by Vishal et al. (2019) four days before E-19A. We use $m_{AB} - m_{Vega} = 1.85$ (Blanton & Roweis 2007).

^b Derived from the flux calibrated spectra and comparison with E-19A (see Sect. 2.2).

spond to the two radio-loud phases (2019 and 2023; four epochs each; see Fig. 1) and these were performed with the NIR arm (10200–24750 Å) of the X-shooter Echelle spectrograph (Vernet et al. 2011) attached to the Very Large Telescope (VLT; Cerro Paranal, Chile). The remaining ten observing epochs were obtained during radio-quiet phases using the EMIR spectrograph (Garzón et al. 2022) at the 10.4-m Gran Telescopio Canarias (GTC; La Palma, Spain).

Each of the VLT/X-shooter epochs consist of 16 exposures, with total exposure times ranging from 1920 to 2400 s, and a slit width of 0.9 arcsec, yielding a spectral resolution of ~ 54 km s⁻¹. The data were processed and calibrated in wavelength and flux using the X-shooter ESO pipeline v. 3.5.0.

For the GTC/EMIR epochs, we obtained eight exposures per observation with the K grism (20270–23730 Å). The total exposure time per observation was 1280 s in 2018 and 1600 s in 2021 and 2022. We used a slit widths of 0.8 and 1.0 arcsec, which give spectral resolutions of ~ 82 km s⁻¹ and ~ 103 km s⁻¹, respectively. The data were reduced using the EMIR Data Reduction Pipeline PyEMIR v. 0.15 (Pascual et al. 2010; Cardiel et al. 2019). The wavelength calibration was carried out using the OH sky lines and verified with the arc lamp files.

The VLT and GTC spectra were corrected for telluric absorption lines using MOLECFIT v. 1.5.9 and v. 3.0.3 (Smette et al. 2015) following the method described in Sánchez-Sierras et al. (2023). The data analysis was performed using MOLLY and custom routines (PYTHON 3.7). Table 1 includes the equivalent width (EW) and the full-width at half maximum (FWHM) of Bry emission

line (21655 Å) for every epoch. The latter was measured from a Gaussian fit to the line profile.

In order to increase the signal-to-noise ratio of the GTC/EMIR spectra, we grouped observations obtained close in time into single epochs. Prior to this, we checked that the Bry line profiles were consistent within each epoch. Thus, E-22A includes two observations, while E-21B and E-22C contain three observations each (Table 1). On the other hand, the VLT/X-shooter epochs correspond to a single observing night. In an attempt to search for possible short-term variability, we also tried dividing each 40-min epoch into eight 5-min spectra, but we did not find any clear evidence for it (e.g. see Fig. A.9 for epoch E-19C). Therefore, only the average spectrum of each GTC and VLT epoch is discussed hereafter (see Table 1).

2.2. K-band photometry

Table 1 includes the K_s magnitude of the system for each spectroscopic epoch. Those corresponding to GTC observations were obtained, when possible, from the EMIR acquisition images.

The X-shooter acquisition is performed in the optical bands. In order to estimate the NIR flux, we have taken the following steps. First, we assigned the K_s AB magnitude (14.18 ± 0.03) reported in Vishal et al. (2019) to E-19A. This was obtained only four days before E-19A. Second, we multiplied each flux-calibrated spectrum by the K_s filter transmission curve and integrated the resulting flux. Finally, we determined the K_s magnitude for each epoch, using that of E-19A as a reference. This

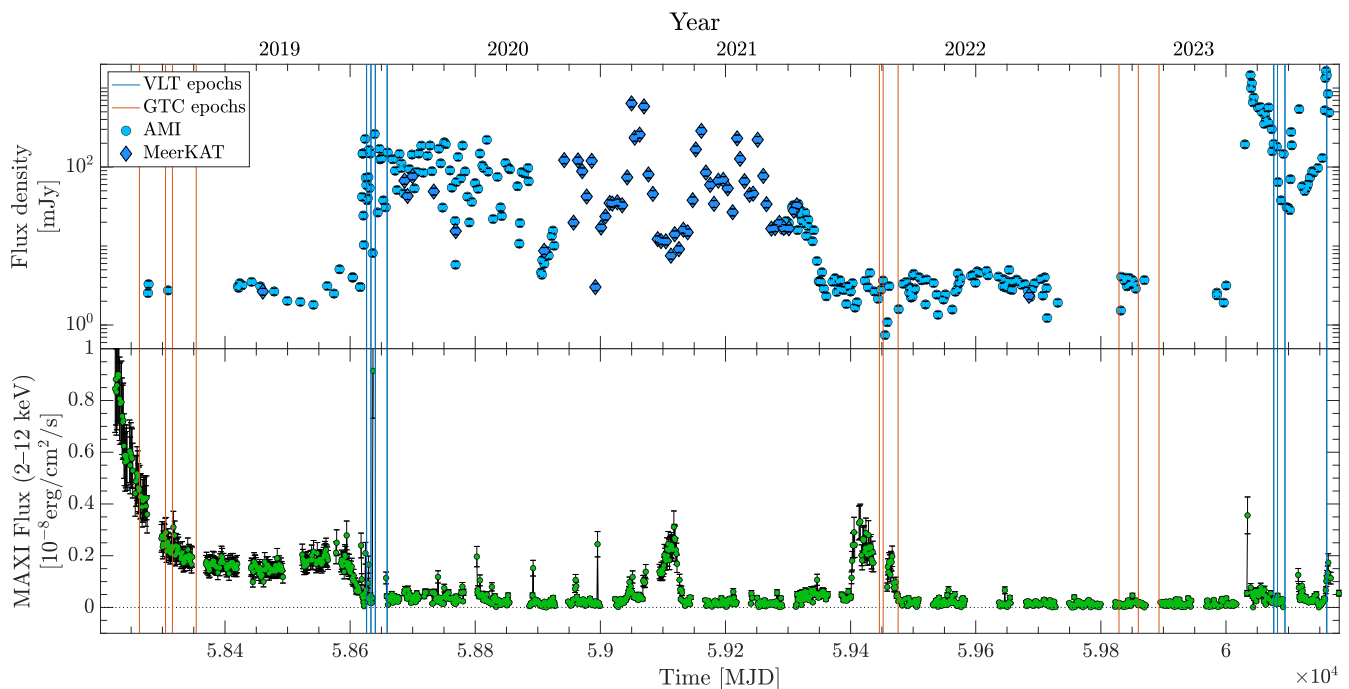


Fig. 1. Light curves in radio (MeerKAT and AMI; top panel) and X-rays (MAXI; bottom panel) from March 2018 (MJD 58200) to August 2023 (MJD 60170). Vertical lines indicate the spectroscopic epochs of GTC/EMIR (orange) and VLT/X-shooter (blue).

method might be affected by systematic errors, as it relies on the spectral flux calibration. Nevertheless, the resulting magnitudes indicate that the radio-loud events are associated with higher NIR fluxes (see Table 1). Furthermore, it shows that the 2023 radio-loud event (Fig. 1) was brighter both in the NIR and in the NIR.

2.3. X-ray and radio monitoring

We extracted the 2018–2023 X-ray light curve in the 2–12 keV interval from data and procedures¹ provided by MAXI (Matsuoka et al. 2009). The resulting light curve with one day bin size is shown in Fig. 1.

We also used radio data obtained with the AMI during 2018–2020 (15.5 GHz; Zwart et al. 2008) and MeerKAT (1.28 GHz; Fender et al. 2016) arrays, as presented in Motta et al. (2021). These have been supplemented by new AMI observations covering the evolution of the system until August 2023. The data have been processed and reduced in the same way as described in Motta et al. (2021). Table 1 labels the X-ray (high, flare and low) and radio (loud, quiet) behaviour at the time of each spectroscopic epoch (based on Fig. 1).

3. Analysis and results

The 18 spectroscopic epochs presented in this work cover the evolution of GRS 1915+105 from May 2018 to August 2023 (Table 1). During this time, we identified four different stages of radio and X-ray activity, which are also associated with significant changes in the NIR spectrum. We discuss them in turn below.

3.1. X-ray decay

After more than 25 years of intense X-ray activity, GRS 1915+105 entered a new phase characterised by a gradual decrease of the X-ray flux, reaching a low-luminosity plateau in 2018 (MJD 58350; Fig. 1). Epochs E-18A and E-18B (GTC), still taken during a phase of relatively high X-ray activity, are characterised by a fairly strong asymmetric Bry line in emission ($EW \sim 10 \text{ \AA}$; see Table 1). The line also shows a hint of a narrow double-peaked profile. The EW of Bry decreased in E-18C and E-18D (down to ~ 6.5 and 4 \AA , respectively), also developing a more pronounced double-peak (Table 1 and Fig. 2). These profiles are commonly interpreted as signalling the presence of an accretion disc (Smak 1969). In this context, the evolution from E-18A to E-18D is consistent with the outer accretion disc responding to the observed drop in X-rays. Thus, as the irradiating X-ray emission decreases, the line-forming region shifts towards inner, higher-velocity regions of the disc, producing less-intense profiles and larger double-peak separations. This behaviour is commonly observed in optical and NIR emission lines of XRB transients when approaching quiescence (e.g. Casares 2015).

3.2. 2019–2021 radio-loud phase

The next significant change was observed in May 2019 (MJD \sim 58600). This involved a further dimming of the X-ray emission, but this time it was accompanied by an increase in the radio flux (Fig. 1), reaching pre-2018 levels (Motta et al. 2021), and in the NIR emission (from $K_s \sim 14.5$ to 13.6, see Table 1). Four VLT/X-shooter epochs were taken during the first month of this radio-loud phase (E-19A to E-19D). These spectra are very rich in emission lines, from He I–10830 to Bry (21655 \AA), with highly variable properties (Fig. 3). Given the high quality spectra and the accurate telluric correction, we even detect the Pa α line

¹ <http://maxi.riken.jp/mxondem/>

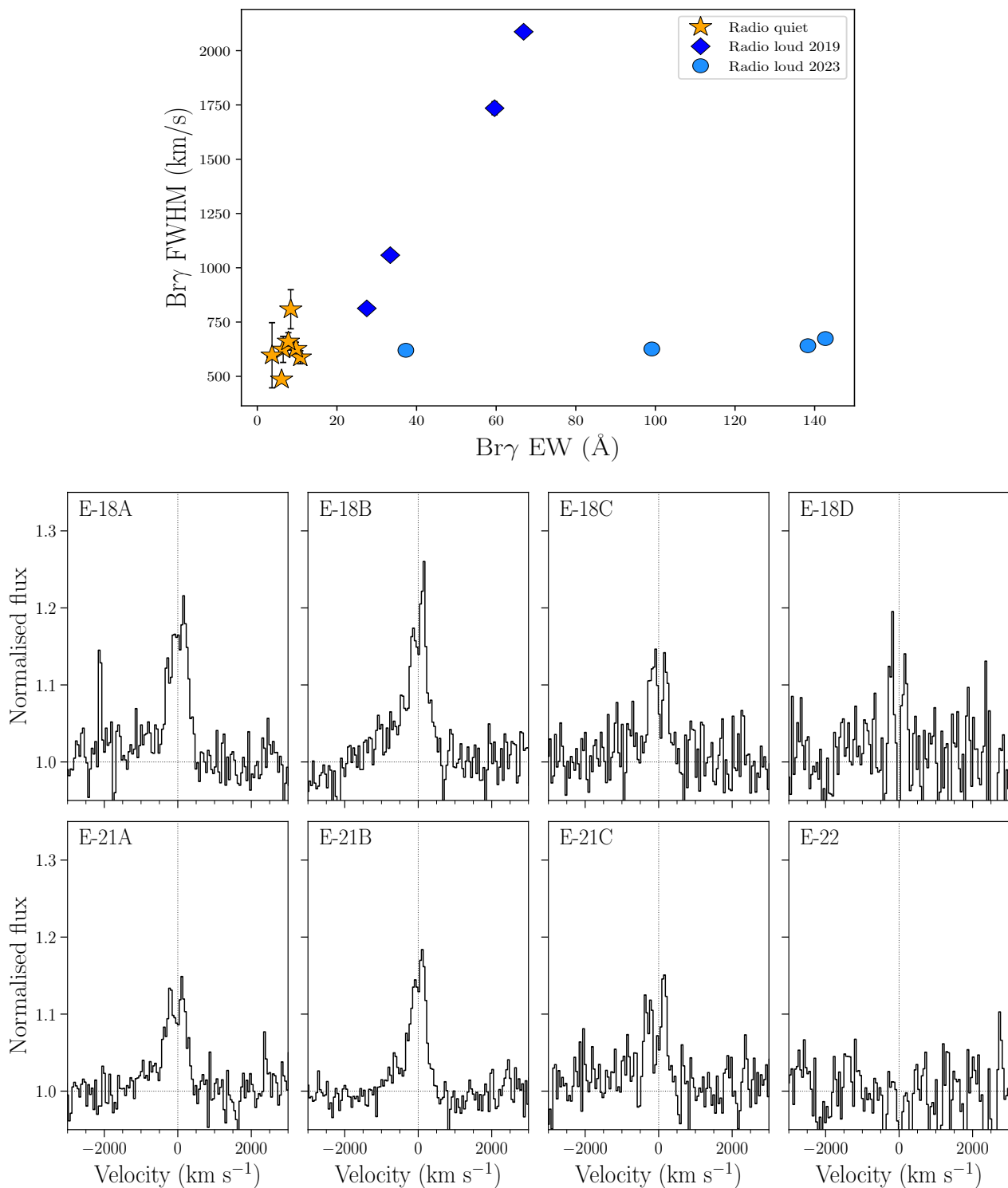


Fig. 2. Evolution of the Br γ emission line. *Top panel:* EW vs FWHM for Br γ line. *Bottom panels:* evolution of the Br γ line profile as observed by GTC/EMIR. We note that E-22 correspond to the mean of the data from the three 2022 epochs.

and high-order Pfund transitions in emission (middle and bottom panels in Figs. A.1-A.4). These features are usually difficult to detect from ground-based observatories since they are affected by strong telluric bands.

Compared to E-18A-D, the EW of Br γ increases dramatically to $\sim 67 \text{ \AA}$ in E-19A, becoming single-peaked but with very broad wings that extend to a full width at zero intensity of $\sim 6000 \text{ km s}^{-1}$. This behaviour is also seen in other Brackett

lines and He I transitions (see Fig. 3). Even more striking is the evidence of conspicuous P-Cygni line profiles only one week later (epochs E-19B and E-19C), indicating the presence of a wind-type outflow (e.g. Castor & Lamers 1979). These profiles are detected in the main He I lines, reaching terminal velocities (hereafter defined as the blue-edge of the blue-shifted absorption) of $\sim 3000 \text{ km s}^{-1}$. The left panels in Fig. 4 show examples of these features (see also Fig. 3). The deepest P-Cygni profile

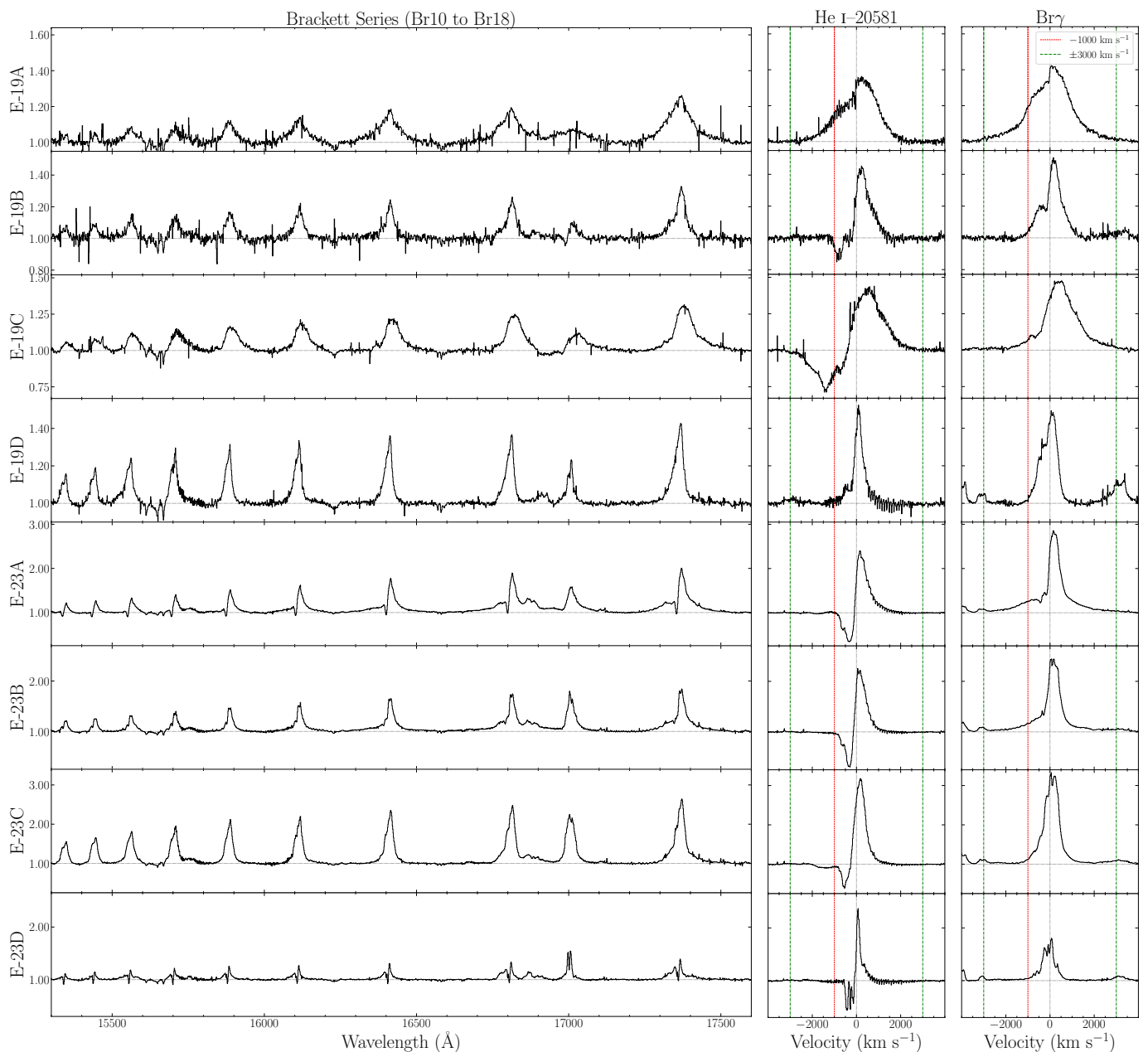


Fig. 3. High order transitions of Brackett Series, He I-20581 and Br γ during the eight epochs observed by VLT/X-shooter. We note that vertical scales are different for every epoch. Red (dashed) and green (dash-dotted) vertical lines indicate velocities of -1000 km s^{-1} and $\pm 3000 \text{ km s}^{-1}$, respectively.

is seen in He I-20581, which shows a blue-shifted absorption reaching $\sim 30\%$ below the continuum level. In addition, we also detect P-Cygni-like features in He I-10830, and He I-21120, all of them with similar terminal velocities. No obvious P-Cygni profiles were detected during E-19D, although the emission lines remain strong and have complex profiles (e.g. skewed towards the red). In addition, two emission lines are detected in E-19D at ~ 21370 and $\sim 21435 \text{ \AA}$, which we identify as Mg II transitions. These transitions have been previously seen in hot stars such as early-B supergiants (Hanson et al. 2005). These are also weakly detected in epochs E-23A-D.

3.3. 2021–2023 radio-quiet phase

The system returned to lower radio flux levels (i.e. similar to those of early 2019) in May 2021, and remained in this regime until April 2023 ($\sim \text{MJD } 59350$; Fig. 1). In turn, the X-ray flux remained at the lowest values most of the time. The notable exceptions to this are the X-ray flares detected around MJD 59100 and 59400 (see Fig. 1; Motta et al. 2021). In particular, the latter flare occurred at the beginning of this radio-quiet period and was covered by three GTC/EMIR epochs: E-21A and E-21B during the flare, while E-21C just after the event. The first two (particularly E-21B) show a Br γ emission line profile very reminiscent of that of E-18A-B (i.e. still during the X-ray active phase), albeit less intense (Fig. 2). By contrast, E-21C is very similar to E-18C-D, with a pronounced double-peaked line profile (see Fig. 2 and Table 1). This evolution is consistent with the outer accre-

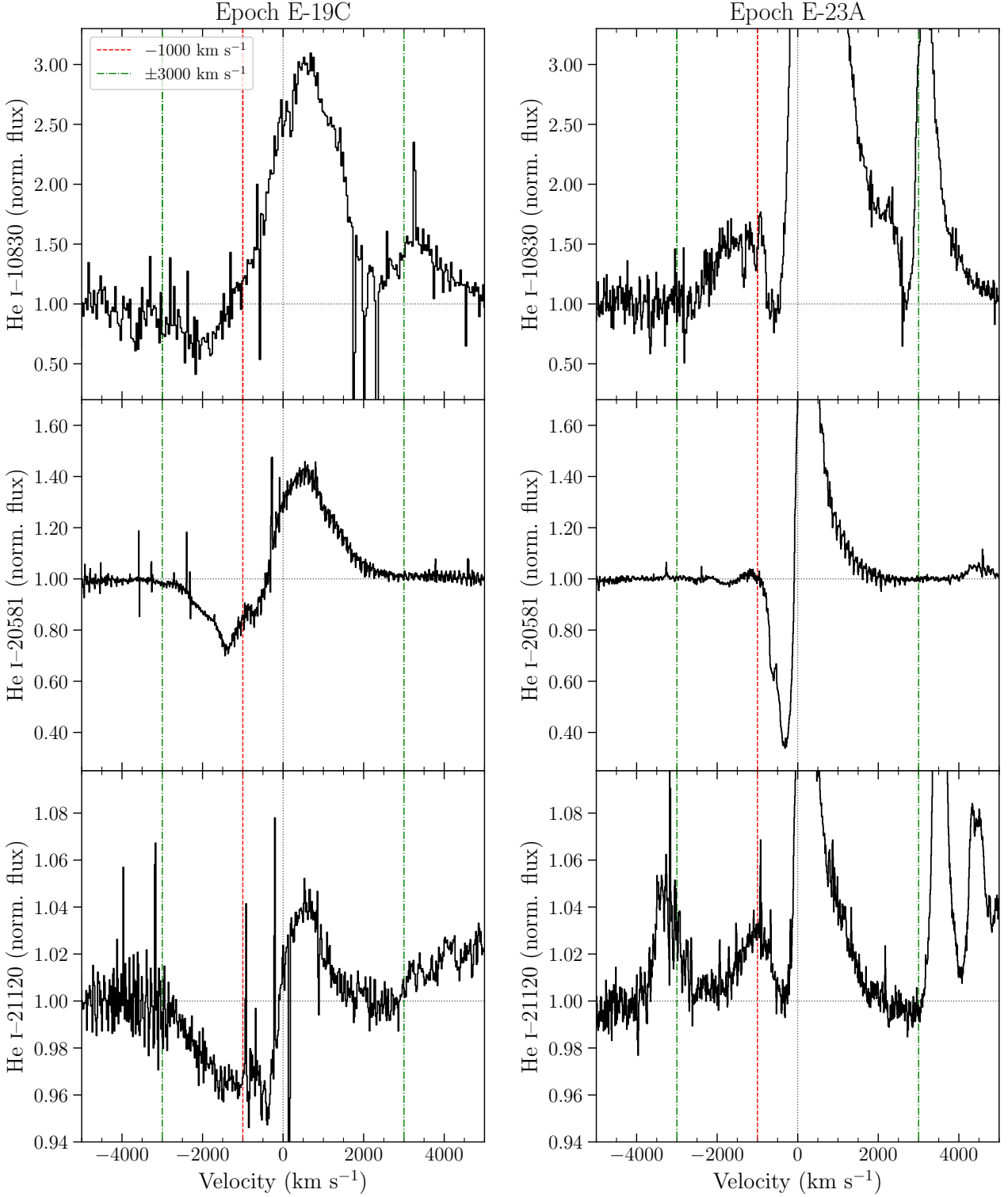


Fig. 4. He I line profiles (10830 Å, 20581 Å and 21120 Å) during epochs E-19C (left) and E-23A (right). Vertical lines are the same as in Fig. 3.

tion disc (traced by the Bry emission) responding to the changes in the observed X-ray flux.

We took three additional GTC/EMIR epochs (E-22A to E-22C) during late 2022. They all show a featureless spectrum, from which we determine a 3σ upper limit to the Bry EW of 0.17 Å (see averaged spectrum in Fig. 2). GRS 1915+105 reached the faintest NIR emission during these epochs with $K_s \sim 15$.

3.4. 2023 radio-loud phase

A new episode of enhanced radio emission at low X-ray flux started in April 2023 (Eggen et al. 2023). Four VLT/X-shooter spectra were obtained during this phase (May to August 2023). These are qualitatively similar to those from 2019 (see Figs. A.5 to A.8). First, the P-Cygni line profiles are detected in He I transitions (see Fig. 4, right panel) with blue-shifted absorptions

reaching depths below $\sim 60\%$ of the continuum level in some cases (e.g. E-23A; see Fig. 4, middle-right panel). The terminal velocities are $\sim 1000 \text{ km s}^{-1}$ ($\sim 750 \text{ km s}^{-1}$ in E-23D), significantly lower than in 2019. Second, broad emission line wings are detected in the Brackett series (Fig. 3, bottom panels), which also show blue absorption troughs during E-23A and E-23D. The emission features are also narrower than in 2019 (see top panel of Fig. 2). However, in E-23A and E-23B, there are additional emission components that are broader (see Bry in Fig. 3), meeting the continuum at $\sim 3000 \text{ km s}^{-1}$. Finally, it is worth mentioning the particularly complex line profiles observed in E-23D, with additional emission peaks (e.g. Bry), noting that some of them found within the blue-shifted absorption of the P-Cygni profiles (e.g. He I–20581). Interestingly, this last spectrum is contemporaneous with a weak X-ray flare (Fig. 1).

4. Discussion

4.1. NIR outflows during the radio-loud phases

The VLT/X-shooter epochs (2019 and 2023), taken during radio-loud phases at low X-ray flux, exhibit wind-type outflows. This is evident from the presence of strong P-Cygni profiles, particularly in the NIR He I transitions. Optical P-Cygni profiles with comparably deep blue-shifted absorptions (i.e. $>30\%$ below the continuum level) have also been observed in V404 Cyg and V4641 Sgr (Muñoz-Darias et al. 2016, 2017, 2018). Together with GRS 1915+105, these systems have the longest orbital periods and, therefore, the largest accretion discs among BH transients. Furthermore, they exhibited the fastest cold (optical/infrared) winds among XRBs ($\sim 3000 \text{ km s}^{-1}$; see e.g. Panizo-Espinar et al. 2022). In addition, V404 Cyg and V4641 Sgr displayed high levels of intrinsic X-ray absorption (e.g. Morningstar & Miller 2014; Motta et al. 2017a; Koljonen & Tomsick 2020), as is the case for GRS 1915+105 during the radio-loud phases ($N_{\text{H}} \sim 7 \times 10^{23} \text{ cm}^{-2}$; Balakrishnan et al. 2021; Miller et al. 2020; Motta et al. 2021).

The NIR signatures of accretion disc winds have been detected in other BH transients, such as MAXI J1820+070 (Sánchez-Sierras & Muñoz-Darias 2020), MAXI J1348-630 (Panizo-Espinar et al. 2022), and MAXI J1803-298 (Mata Sánchez et al. 2022). However, the NIR P-Cygni profiles reported in this work are the most prominent seen in a BH transient to date. The observational appearance of the wind in GRS 1915+105 differs between 2019 and 2023. In 2019, we measure larger blue-edge velocities in the P-Cygni profiles, reaching $\sim 3000 \text{ km s}^{-1}$, whereas in 2023 some emission lines (e.g. Brackett series) displayed additional emission components with blue wings meeting the continuum at $\sim 3000 \text{ km s}^{-1}$. This combination of blue-shifted absorptions and enhanced emission at the same velocities has been observed in other systems and may be related to the optical depth of the ejecta (e.g. Fig. 15 in Mata Sánchez et al. 2018). Furthermore, the evolution of the EW and FWHM of the Bry line (top panel in Fig. 2) is significantly different between 2019 and 2023. Comparing this behaviour with that of H α during the 2015 outburst of V404 Cyg (Fig. 9 in Mata Sánchez et al. 2018), we are able to identify the 2019 spectra with the phase of strongest P-Cygni signatures, while the evolution during 2023 might be characterised by optically thinner ejecta. Finally, in 2023, we observe increased radio brightness and more intense Bry lines, as compared to 2019, resembling the early outburst behaviour noted by Eikenberry et al. (1998).

4.2. A massive, multi-phase wind

In this work, we have discovered strong NIR outflow signatures in GRS 1915+105 at low X-ray fluxes. However, weaker (tentative) NIR detections had previously been reported at much higher X-ray fluxes (e.g. Mirabel et al. 1997; Martí et al. 2000). Conversely, hot winds at similar velocities than those reported here have been widely observed in the source (e.g. Kotani et al. 2000; Lee et al. 2002; Ueda et al. 2009; Neilsen et al. 2011) during the (X-ray) bright phases.

X-ray accretion disc winds were convincingly detected during the onset of the 2019 radio-loud event (Miller et al. 2020), 24 days before our first NIR wind detection (E-19A). However, the characteristic velocity of this hot wind was $\sim 300 \text{ km s}^{-1}$, which is an order of magnitude lower than that of the NIR wind and previous X-ray detections. This is consistent with the idea that accretion disc winds in XRBs are multi-phase in nature, with a variable balance between the different phases (e.g. hot and cold) depending on the physical conditions of the ejecta. This scenario is supported by the observation of both X-ray and optical winds in V404 Cyg (Muñoz-Darias & Ponti 2022). Thus, contemporaneous observations at low and high energies are likely the most effective approach for gaining a deeper understanding of the observational properties of the wind. In this regard, a mass outflow rate comparable to the accretion rate was roughly estimated for the low-velocity X-ray wind (Miller et al. 2020); however, this could be increased by an order of magnitude if the NIR wind velocity were to be used instead. This would suggest a massive, outflowing wind, which is consistent with previous estimations for this system (e.g. Neilsen et al. 2011) and V404 Cyg (Muñoz-Darias et al. 2016; Casares et al. 2019).

4.3. Long-term evolution of GRS 1915+105 and the nature of the radio-loud events

The evolution of the Bry line during the radio-quiet epochs indicates that the properties of the line respond to the observed X-ray flux. For instance, we observe the line weakening and the peak-to-peak separation of the profile increasing as the system becomes fainter in X-rays, a behaviour typically observed in XRB transients when approaching quiescence. This is consistent with the X-ray fitting by Motta et al. (2021), which shows no indication of enhanced intrinsic absorption during the radio-quiet phase. The NIR continuum also follows this trend, with the second radio-quiet period (i.e. 2022) being fainter in the NIR than the first one (~ 2019). This makes even more significant the lack of Bry emission in E-22A to E-22C, since the diluting continuum is also weaker. Featureless NIR spectra have been seen in BH hard states at very low luminosity (e.g. Sánchez-Sierras & Muñoz-Darias 2020) and might indicate a dominant jet contribution. All things considered, if the radio-loud epochs are excluded, the behaviour of GRS 1915+105 since 2018 is in line with a gradual decline from its long and luminous outburst, potentially heading towards quiescent levels. However, we must consider how the radio-loud epochs fit in this scenario.

A first-order explanation for the radio-loud phases is that they are associated with a severe increase of the accretion rate. The source would remain faint in X-rays as a result of very high intrinsic absorption (Miller et al. 2020; Motta et al. 2021). In this scenario, the radio-loud phases may correspond to mini-outbursts, also known as secondary outbursts or re-brightenings, which are commonly observed in XRB transients during the decay phase of a main outburst (e.g. Callanan et al. 1995; Jonker et al. 2012; Cúneo et al. 2020). These secondary events tend to

be progressively shorter and fainter than the main event (e.g. ~ 250 day-long outburst and 25–30 day-long reflares in MAXI J1820+070; Stiele & Kong 2020). In the case of GRS 1915+105, the first radio-loud event lasted two years, much less than the 25-year main outburst. However, the high associated radio fluxes (record breaking in 2023; see Trushkin et al. 2023) may challenge this scenario if they are tracing the actual X-ray (i.e. accretion) luminosity. Nevertheless, it is important to consider that GRS 1915+105 is a unique system in many respects and the behaviour of its large accretion disc may deviate from the norm also during this potentially last phase of the outburst.

5. Conclusions

In this work, we present NIR spectroscopy covering the evolution of GRS 1915+105 from the start of its X-ray decline in 2018. Our results reveal the presence of strong NIR winds during two radio-loud phases displayed by the system, with terminal velocities of up to ~ 3000 km s⁻¹. These outflows are contemporaneous with high intrinsic X-ray absorption. A similar behaviour has been observed in other BH transients, in particular, V404 Cyg and V4641 Sgr. This reinforces the idea that massive and multi-phase outflows, which are potentially able to obscure the source in X-rays, are a distinctive feature of the largest BH accretion discs. In addition, the evolution of the Br γ emission line during radio-quiet phases is consistent with the low X-ray flux displayed by the source. This study highlights the importance of NIR spectroscopy in the study of BH transients and should be complemented with future investigations on the evolution of this critical system across various wavelengths.

Acknowledgements. We are thankful to the anonymous referee for helpful comments that improved the paper. This work is supported by the Spanish Ministry of Science via an *Europa Excelencia* grant (EUR2021-122010) and the *Plan de Generacion de conocimiento*: PID2020-120323GB-I00 and PID2021-124879NB-I00. JAFO acknowledges financial support by the Spanish Ministry of Science and Innovation (MCIN/AEI/10.13039/501100011033) and “ERDF A way of making Europe” through the grant PID2021-124918NB-C44; MCIN and the European Union – NextGenerationEU through the Recovery and Resilience Facility project ICTS-MRR-2021-03-CEFCA. We are thankful to the GTC staff, in particular Antonio L. Cabrera Lavers, for their useful help to perform the spectroscopic observations presented in this letter. Based on observations carried out with the EMIR spectrograph under programmes GTC38-18A and GTC55-21A. Based on data from the GTC Archive at CAB (INTA-CSIC). Based on observations collected at the European Southern Observatory under ESO programmes 103.200K.001 and 111.2649.001. We thank the staff of the Mullard Radio Astronomy Observatory, University of Cambridge, for their support in the maintenance and operation of AMI, which is supported by the Universities of Cambridge and Oxford. We also acknowledge support from the European Research Council under grant ERC-2012-StG-307215 LODESTONE. We thank the staff at the South African Radio Astronomy Observatory (SARAO) for scheduling the MeerKAT observations. The MeerKAT telescope is operated by the South African Radio Astronomy Observatory, which is a facility of the National Research Foundation, an agency of the Department of Science and Innovation. This research has made use of MAXI data provided by RIKEN, JAXA and the MAXI team. MOLLY software developed by Tom Marsh is gratefully acknowledged.

References

Balakrishnan, M., Miller, J. M., Reynolds, M. T., et al. 2021, *ApJ*, 909, 41
 Blanton, M. R. & Roweis, S. 2007, *AJ*, 133, 734
 Callanan, P. J., Garcia, M. R., McClintock, J. E., et al. 1995, *ApJ*, 441, 786
 Cardiel, N., Pascual, S., Gallego, J., et al. 2019, *Aspc*, 523, 317
 Casares, J. 2015, *ApJ*, 808, 80
 Casares, J., Muñoz-Darias, T., Mata Sánchez, D., et al. 2019, *MNRAS*, 488, 1356
 Castor, J. I. & Lamers, H. J. G. L. M. 1979, *ApJS*, 39, 481
 Castro-Tirado, A. J., Brandt, S., Lund, N., et al. 1994, *ApJS*, 92, 469
 Chapuis, C. & Corbel, S. 2004, *A&A*, 414, 659
 Corral-Santana, J. M., Casares, J., Muñoz-Darias, T., et al. 2016, *A&A*, 587, A61
 Cúneo, V. A., Alabarta, K., Zhang, L., et al. 2020, *MNRAS*, 496, 1001

Díaz Trigo, M. & Boirin, L. 2016, *Astronomische Nachrichten*, 337, 368
 Egron, E., Rodriguez, J., Trushkin, S. A., et al. 2023, *The Astronomer’s Telegram*, 16008
 Eikenberry, S. S., Matthews, K., Murphy, Jr., T. W., et al. 1998, *ApJ*, 506, L31
 Fender, R. & Belloni, T. 2004, *Annual Review of Astronomy and Astrophysics*, 42, 317
 Fender, R., Woudt, P., Armstrong, R., et al. 2016, *Proceedings of MeerKAT Science: On the Pathway to the SKA*, 13
 Garzón, F., Balcells, M., Gallego, J., et al. 2022, *A&A*, 667, 107
 Hanson, M. M., Kudritzki, R., Kenworthy, M. A., Puls, J., & Tokunaga, A. T. 2005, *ApJS*, 161, 154
 Jonker, P. G., Miller-Jones, J. C., Homan, J., et al. 2012, *MNRAS*, 423, 3308
 Koljonen, K. I. & Tomsick, J. A. 2020, *A&A*, 639, A13
 Kotani, T., Ebisawa, K., Dotani, T., et al. 2000, *ApJ*, 539, 413
 Lee, J. C., Reynolds, C. S., Remillard, R., et al. 2002, *ApJ*, 567, 1102
 Martí, J., Mirabel, I. F., Chaty, S., & Rodríguez, L. F. 2000, *A&A*, 356, 943
 Mata Sánchez, D., Muñoz-Darias, T., Casares, J., et al. 2018, *MNRAS*, 481, 2646
 Mata Sánchez, D., Muñoz-Darias, T., Cúneo, V. A., et al. 2022, *ApJ*, 926, L10
 Matsuoka, M., Kawasaki, K., Ueno, S., et al. 2009, *PASJ*, 61, 999
 Miller, J. M., Zoghbi, A., Raymond, J., et al. 2020, *ApJ*, 904, 30
 Mirabel, I. F., Bandyopadhyay, R., Charles, P. A., Shahbaz, T., & Rodríguez, L. F. 1997, *ApJ*, 477, L45
 Mirabel, I. F. & Rodríguez, L. F. 1994, *Nature*, 371, 46
 Morningstar, W. R. & Miller, J. M. 2014, *ApJ*, 793, L33
 Motta, S. E., Kajava, J. J., Giustini, M., et al. 2021, *MNRAS*, 503, 152
 Motta, S. E., Kajava, J. J. E., Sánchez-Fernández, C., et al. 2017a, *MNRAS*, 471, 1797
 Motta, S. E., Kajava, J. J. E., Sánchez-Fernández, C., Giustini, M., & Kuulkers, E. 2017b, *MNRAS*, 468, 981
 Muñoz-Darias, T., Casares, J., Mata Sánchez, D., et al. 2016, *Nature*, 534, 75
 Muñoz-Darias, T., Casares, J., Mata Sánchez, D., et al. 2017, *MNRAS*, 465, L124
 Muñoz-Darias, T., Jiménez-Ibarra, F., Panizo-Espinar, G., et al. 2019, *ApJ*, 879, L4
 Muñoz-Darias, T. & Ponti, G. 2022, *A&A*, 664, A104
 Muñoz-Darias, T., Torres, M. A. P., & García, M. R. 2018, *MNRAS*, 479, 3987
 Neilsen, J. & Lee, J. C. 2009, *Nature*, 458, 481
 Neilsen, J., Remillard, R. A., & Lee, J. C. 2011, *ApJ*, 737, 69
 Panizo-Espinar, G., Armas Padilla, M., Muñoz-Darias, T., et al. 2022, *A&A*, 664, A100
 Parra, M., Petrucci, P. O., Bianchi, S., et al. 2023 [arXiv:2308.00691]
 Pascual, S., Gallego, J., Cardiel, N., & Eliche-Moral, M. C. 2010, *Aspc*, 434, 353
 Ponti, G., Fender, R. P., Begelman, M. C., et al. 2012, *MNRAS*, 422, L11
 Sánchez-Sierras, J. & Muñoz-Darias, T. 2020, *A&A*, 640, L3
 Sánchez-Sierras, J., Muñoz-Darias, T., Casares, J., et al. 2023, *A&A*, 673, A104
 Smak, J. 1969, *Acta Astron.*, 19, 155
 Smette, A., Sana, H., Noll, S., et al. 2015, *A&A*, 576, A77
 Steeghs, D., McClintock, J. E., Parsons, S. G., et al. 2013, *ApJ*, 768, 185
 Stiele, H. & Kong, A. K. H. 2020, *ApJ*, 889, 142
 Trushkin, S. A., Nizhelskij, N. A., Tsybulev, P. G., & Shevchenko, A. V. 2023, *The Astronomer’s Telegram*, 15974
 Ueda, Y., Yamaoka, K., & Remillard, R. 2009, *ApJ*, 695, 888
 Vernet, J., Dekker, H., D’Odorico, S., et al. 2011, *A&A*, 536, A105
 Vishal, J., Banerjee, Dipankar, K. P., et al. 2019, *The Astronomer’s Telegram*, 12806
 Zwart, J. T., Barker, R. W., Biddulph, P., et al. 2008, *MNRAS*, 391, 1545

Appendix A: Supplementary figures

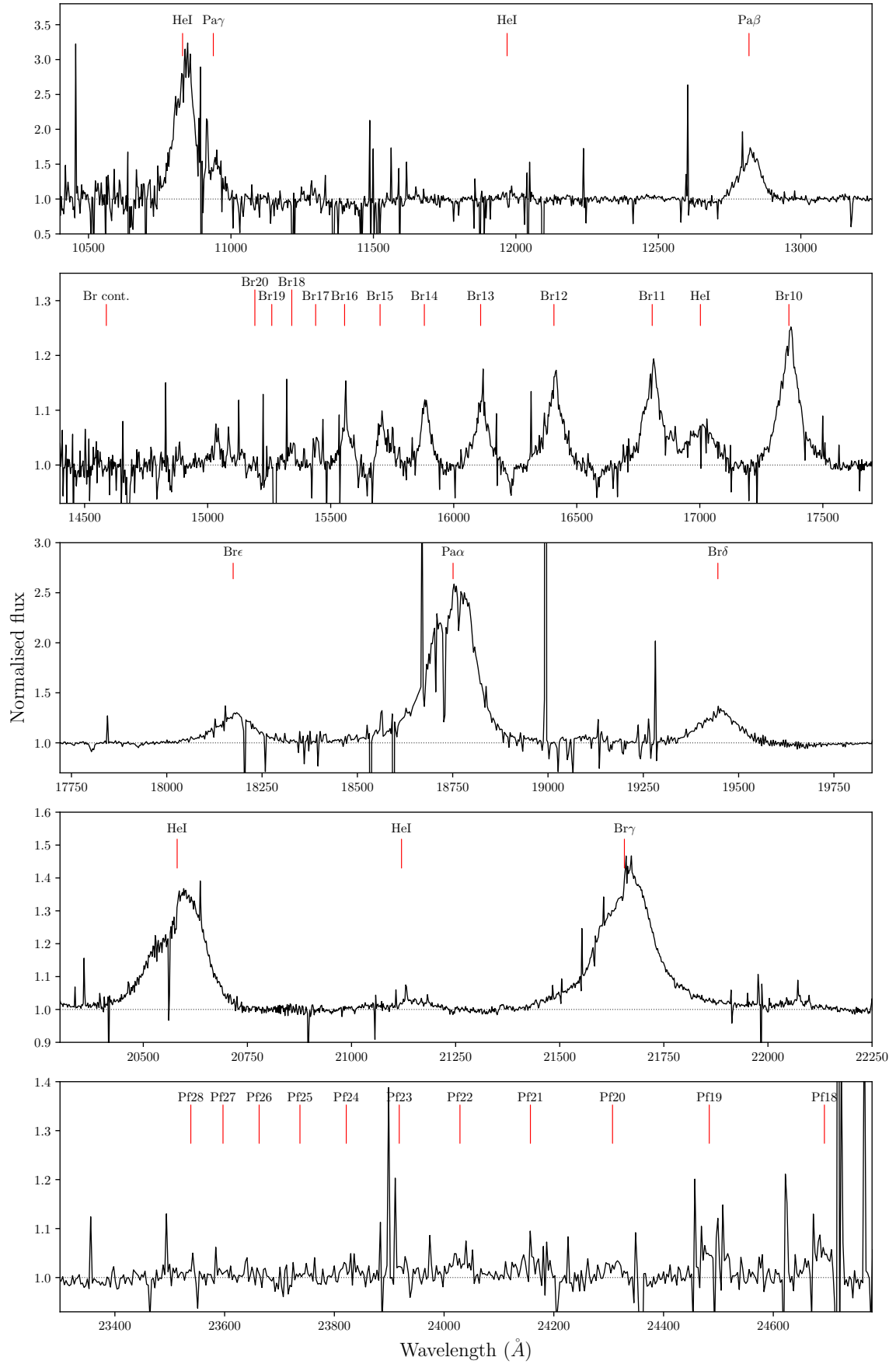


Fig. A.1. Full normalised spectrum of VLT/X-shooter epoch E-19A. *Middle panel:* Pa α in the center alongside with Br δ and Br ϵ . *Bottom panel:* Higher orders of Pfund Series. We note that middle and bottom panels are strong affected by telluric absorptions.

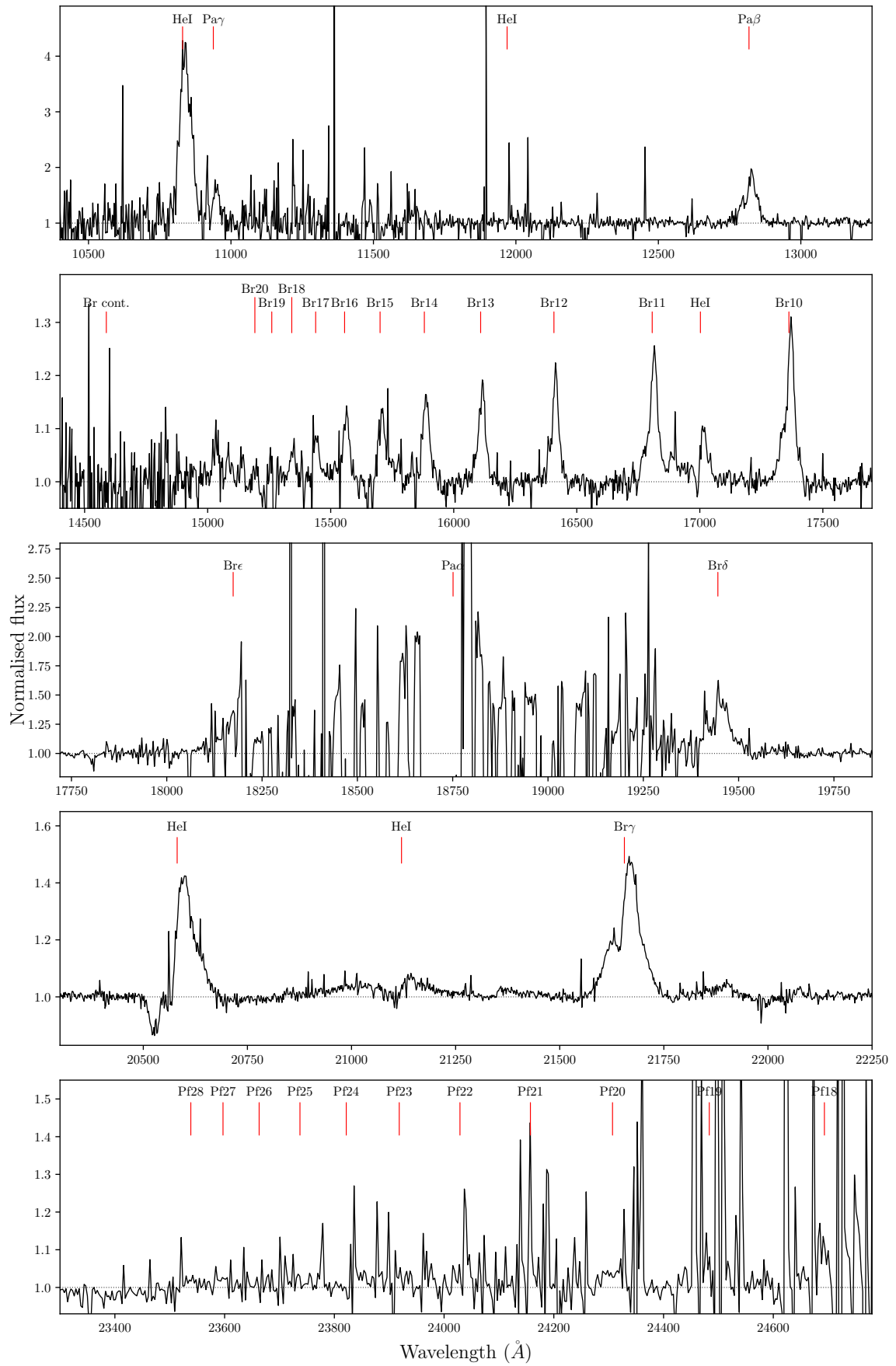


Fig. A.2. Full normalised spectrum of VLT/X-shooter epoch E-19B. *Middle panel:* Pa α in the center alongside with Br δ and Br ϵ . *Bottom panel:* Higher orders of Pfund Series.

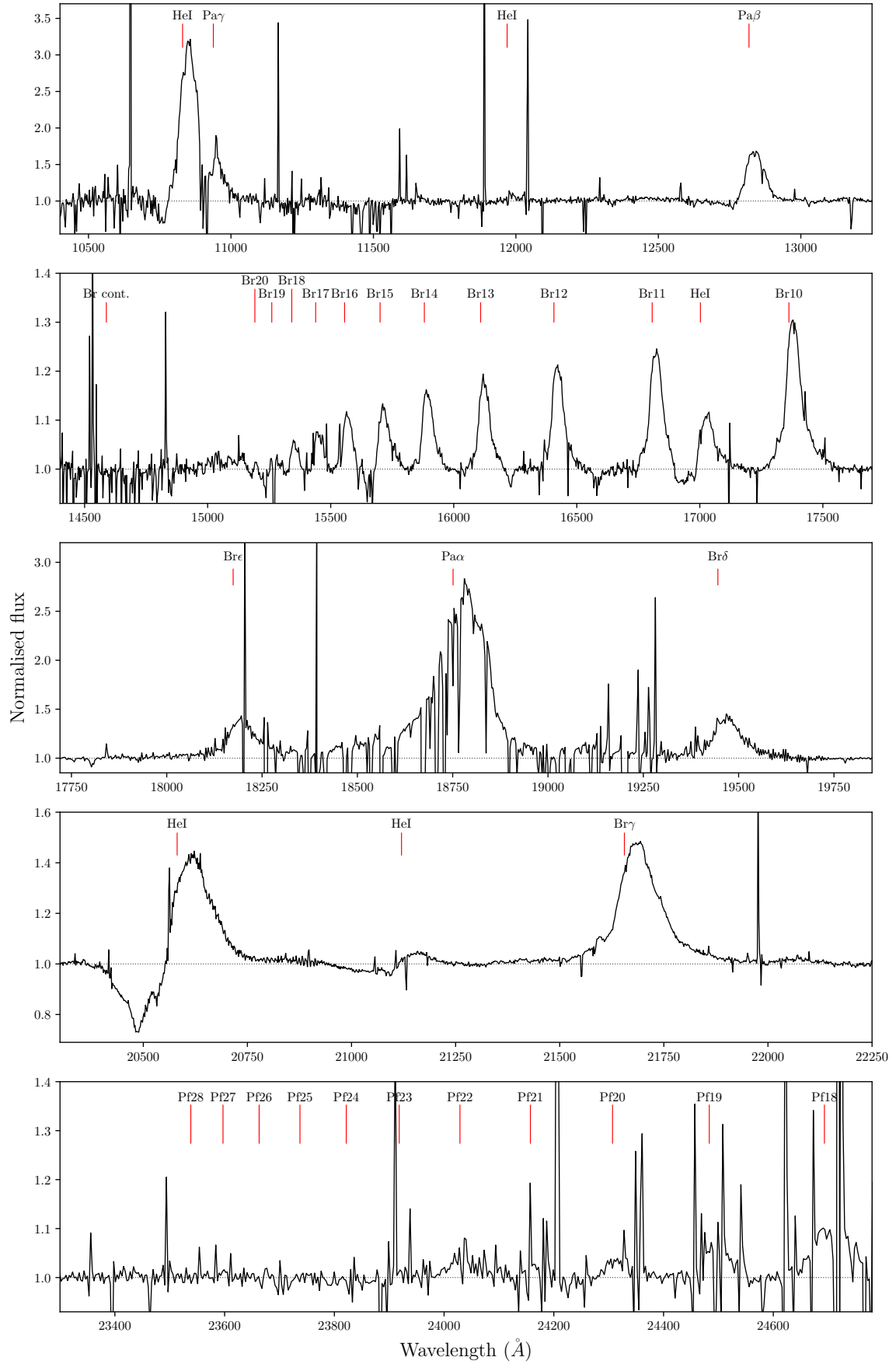


Fig. A.3. Full normalised spectrum of VLT/X-shooter epoch E-19C. *Middle panel:* Pa α in the center alongside with Br δ and Br ϵ . *Bottom panel:* Higher orders of Pfund Series.

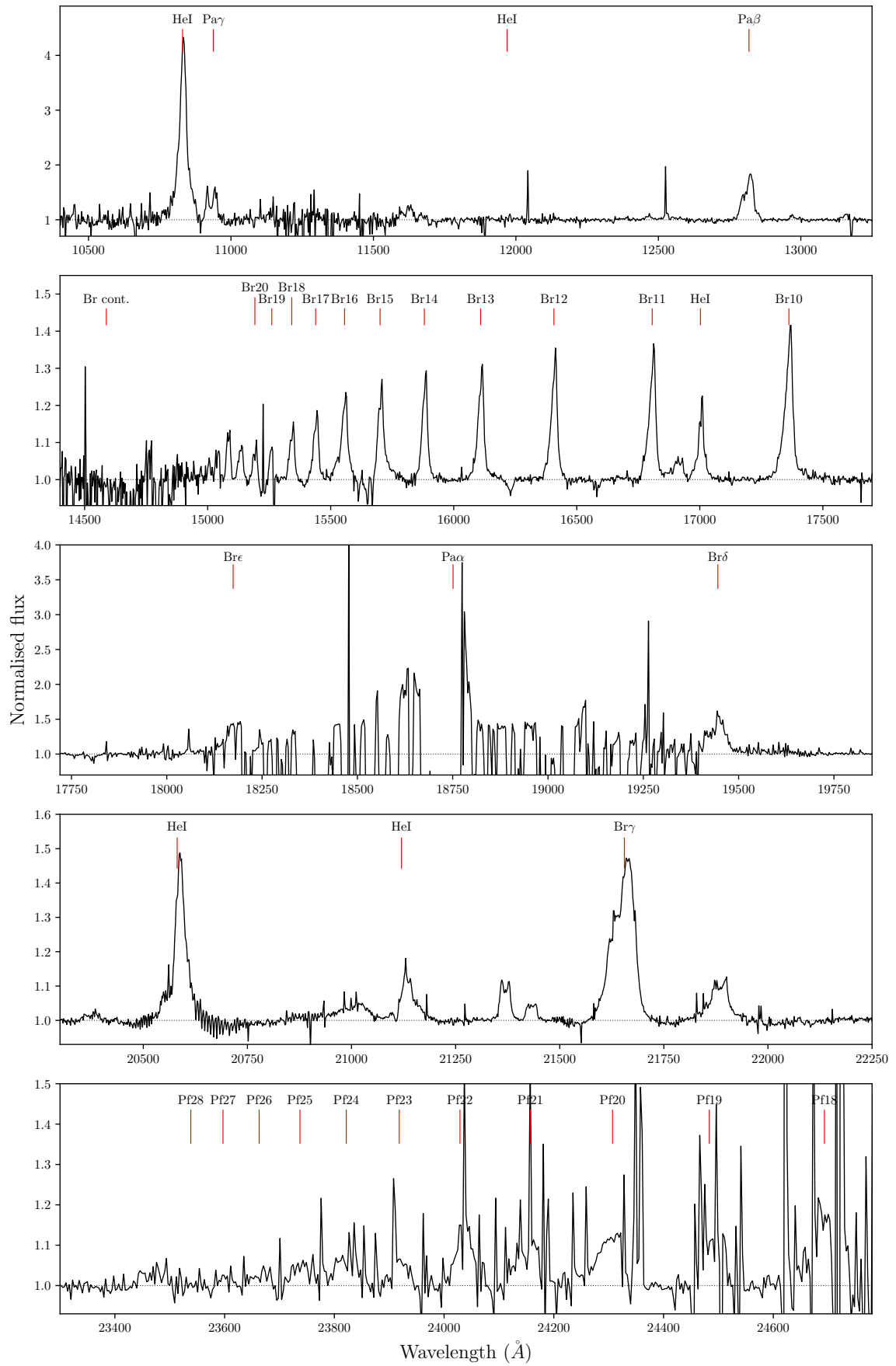


Fig. A.4. Full normalised spectrum of VLT/X-shooter epoch E-19D. *Middle panel:* Pa α in the center alongside with Br δ and Br ϵ . *Bottom panel:* Higher orders of Pfund Series.

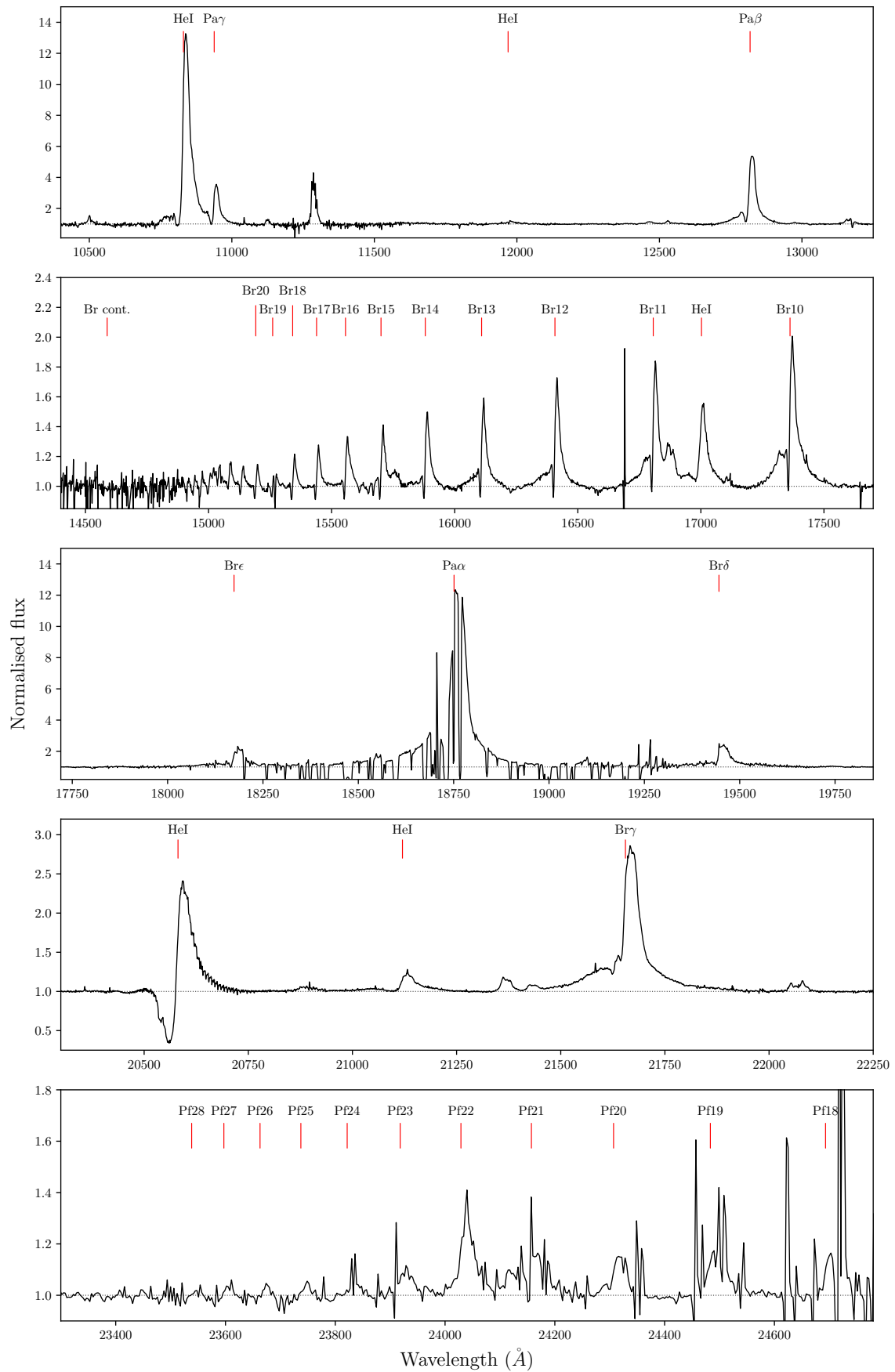


Fig. A.5. Full normalised spectrum of VLT/X-shooter epoch E-23A. *Middle panel:* Pa α in the center alongside with Br δ and Br ϵ . *Bottom panel:* Higher orders of Pfund Series.

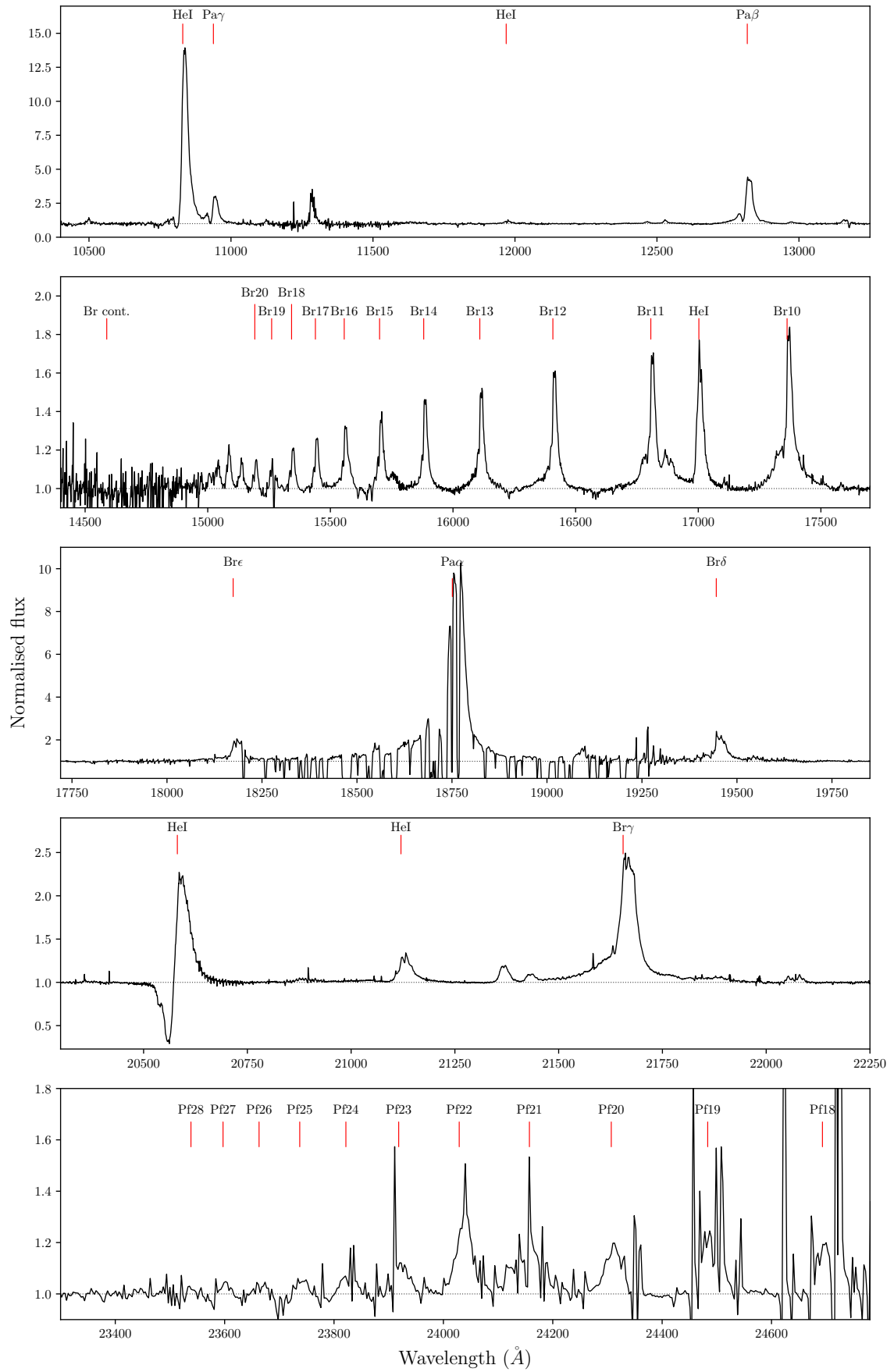


Fig. A.6. Full normalised spectrum of VLT/X-shooter epoch E-23B. *Middle panel:* Pa α in the center alongside with Br δ and Br ϵ . *Bottom panel:* Higher orders of Pfund Series.

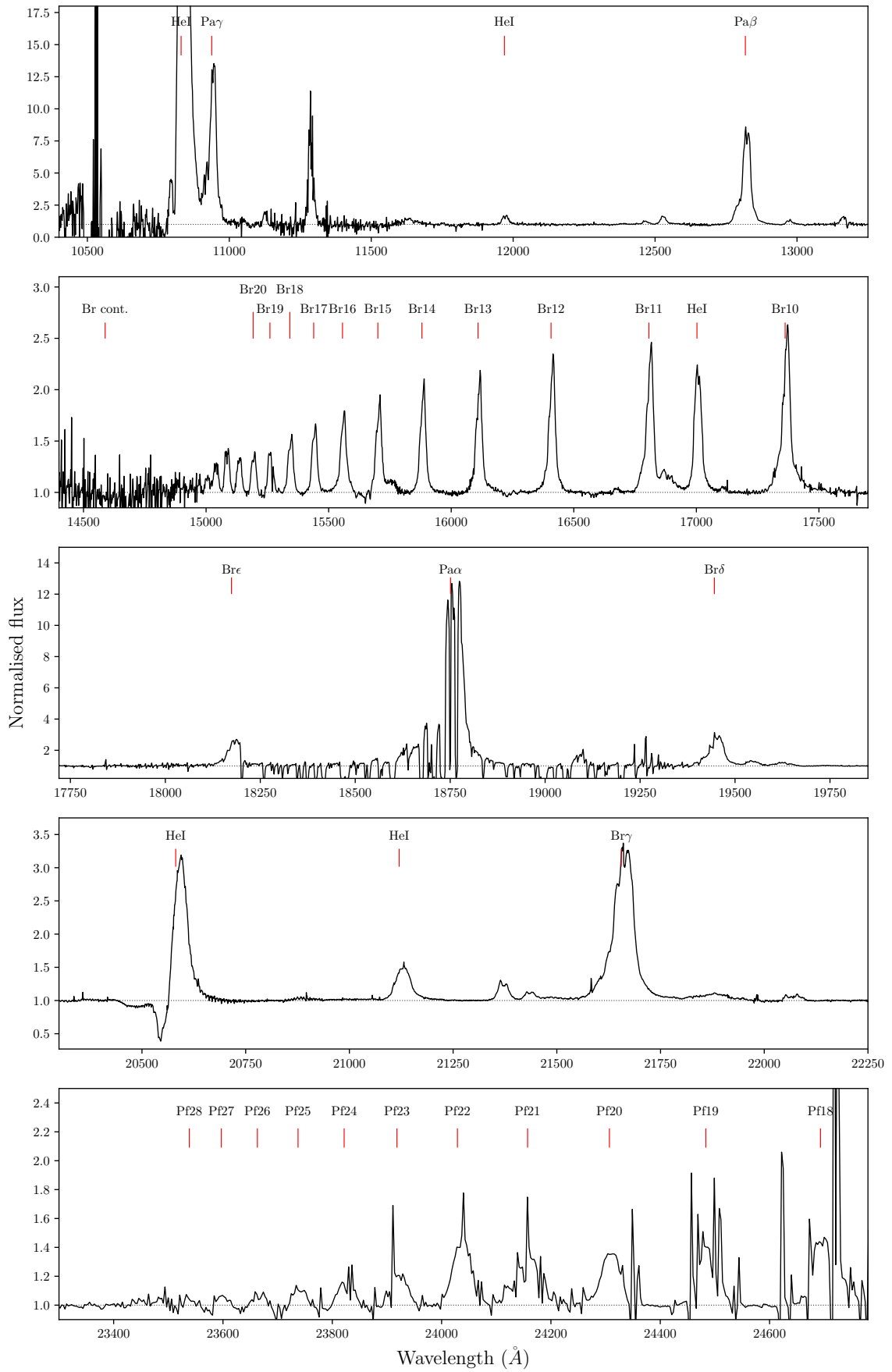


Fig. A.7. Full normalised spectrum of VLT/X-shooter epoch E-23C. *Middle panel:* Pa α in the center alongside with Br δ and Br ϵ . *Bottom panel:* Higher orders of Pfund Series.

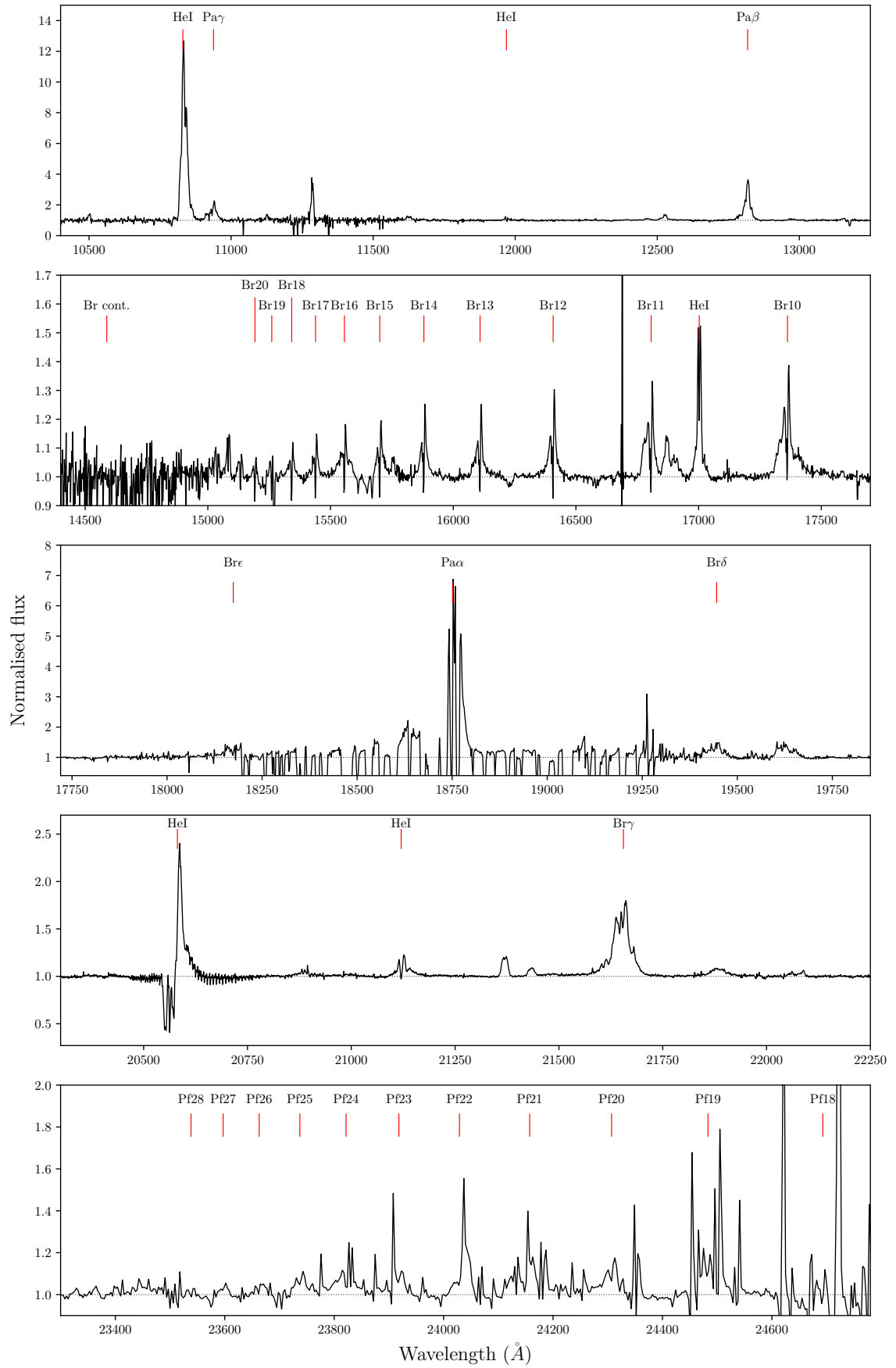


Fig. A.8. Full normalised spectrum of VLT/X-shooter epoch E-23D. *Middle panel:* Pa α in the center alongside with Br δ and Br ϵ . *Bottom panel:* Higher orders of Pfund Series.

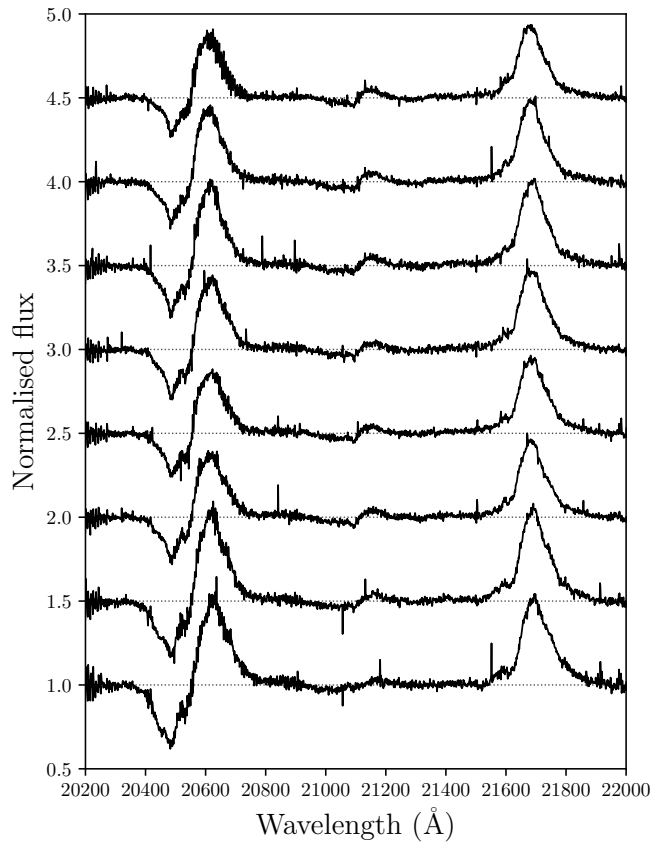


Fig. A.9. K-band region of epoch E-19C (VLT/X-shooter) with high time resolution (5 min each). The epoch has been divided into the eight spectra shown in the figure.